

Relaxation Mode Analysis and Markov State Relaxation Mode Analysis for Chignolin in Aqueous Solution near a Transition Temperature

Ayori Mitsutake^{1,2, a)} and Hiroshi Takano^{1, b)}

¹⁾*Department of Physics, Faculty of Science and Technology, Keio University, Yokohama, Kanagawa 223-8522, Japan*

²⁾*JST, PRESTO, Yokohama, Kanagawa 223-8522, Japan*

It is important to extract reaction coordinates or order parameters from protein simulations in order to investigate the local minimum-energy states and the transitions between them. The most popular method to obtain such data is principal component analysis, which extracts modes of large conformational fluctuations around an average structure. We recently applied relaxation mode analysis for protein systems, which approximately estimates the slow relaxation modes and times from a simulation and enables investigations of the dynamic properties underlying the structural fluctuations of proteins. In this study, we apply this relaxation mode analysis to extract reaction coordinates for a system in which there are large conformational changes such as those commonly observed in protein folding/unfolding. We performed a 750-ns simulation of chignolin protein near its folding transition temperature, and observed many transitions between the most stable, misfolded, intermediate, and unfolded states. We then applied principal component analysis and relaxation mode analysis to the system. In the relaxation mode analysis, we could automatically extract good reaction coordinates. The free-energy surfaces provide a clearer understanding of the transitions not only between local minimum-energy states but also between the folded and unfolded states, even though the simulation involved large conformational changes. Moreover, we propose a new analysis method called Markov state relaxation mode analysis. We applied the new method to states with slow relaxation, which are defined by the free-energy surface obtained in the relaxation mode analysis. Finally, the relaxation times of the states obtained with a simple Markov state model and the proposed Markov state relaxation mode analysis are compared and discussed.

I. INTRODUCTION

Biopolymers have flexible structures and show variable functions. These functions are derived not only from the structure but also from the dynamics of the structural fluctuations themselves. Therefore, identifying the dynamic properties of the structural fluctuations of biopolymers is important for understanding the interrelationship between their movements and functions. Classical molecular dynamics (MD) simulation is a popular and powerful method for describing the structure, dynamics, and function of biomolecules in microscopic detail. Recent technological advances have allowed for simulations to be carried out on the timescales of the order of milliseconds (see reviews by Refs. 1,2). As longer and larger MD simulations are now being performed, it has become more important to develop methods for extracting the most “essential” modes from the trajectory³. Indeed, the development of a method to reduce the huge number of degrees of freedom of coordinates to a few collective degrees of freedom is an active field of theoretical research.

Principal component analysis (PCA), also called quasi-harmonic analysis or the essential dynamics method^{4–10}, is one of the most popular methods for analyzing the static properties of the fluctuations of structures. A system’s fluctuations can be described in terms of only a few principal components (PCs). Moreover, this method

has been widely used to extract the few important collective modes of a biomolecule, which may serve as relevant coordinates of the free-energy surface. However, if the simulation involves large conformational changes such as folding/unfolding simulations, and the conformational changes between local minimum-energy states are small compared with those between the folded and unfolded states, it is difficult for PCA to extract the effective modes or order parameters to identify the local minimum-energy states. The root mean square distance (RMSD) from a reference structure, the radius of gyration, or selected distances, among others, are often used as order parameters to construct free-energy surfaces and analyze the structures obtained from a simulation. The selection of these order parameters depends on the simulation system. To identify the local minimum-energy states from the simulation, suitable order parameters must be considered, which depend on the simulation system. Therefore, given the recent possibility for performing longer MD simulations, a new analysis method must be able to extract suitable order parameters for identifying local minimum-energy states automatically, and for investigating the dynamics and kinetics of proteins.

Relaxation mode analysis (RMA) was developed to investigate the “dynamic” properties of spin systems¹¹ and homopolymer systems^{12,13}, and has been applied to various polymer systems^{14–22} to investigate their slow relaxation dynamics^{23,24}. Recently, RMA has also been applied to biomolecular systems^{25,26}. The relaxation modes and rates are given as left eigenfunctions and eigenvalues of the time-evolution operator of the master equation of

^{a)}Electronic mail: ayori@rk.phys.keio.ac.jp

^{b)}Electronic mail: takano@rk.phys.keio.ac.jp

the system, respectively^{11–13}. The equilibrium time correlation functions of the relaxation modes, $\{X_p\}$, satisfy

$$\langle X_p(t)X_q(0) \rangle = \delta_{p,q}e^{-\lambda_p t}, \quad (1)$$

where $\langle X_p(t)X_q(0) \rangle$ denotes the equilibrium correlation of X_p at time t and X_q at time 0, and λ_p represents the relaxation rate of X_p .

In RMA, we calculate the approximate relaxation modes and rates from a simulation. RMA is formulated as a variational problem equivalent to the eigenvalue problem of the time-evolution operator of the system, where a relaxation mode X_p is approximated by a trial function, which is constructed as a linear combination of relevant physical quantities that are time-evolved for $t_0/2$. The parameter t_0 is introduced in order to reduce the relative weight of the faster modes contained in the physical quantities. The optimization of the normalized equilibrium autocorrelation function of the trial function time-displaced by τ leads to the generalized eigenvalue problem. In practice, the time correlation matrices of structural fluctuations for two different times (t_0 and $t_0 + \tau$) are calculated through simulations. Then, by solving a generalized eigenvalue problem for these matrices, the relaxation rates and modes are obtained from the eigenvalues and eigenvectors, respectively. Thus, we call this method the RMA method using a single evolution time: $t_0/2$.

Recently, RMA was applied to a Monte Carlo simulation for a heteropolymer peptide system with a small number of degrees of freedom²⁵, and its effectiveness was demonstrated. In the applications of RMA to homopolymer systems^{12–19}, the translational degrees of freedom are removed from the conformations of the polymer sampled in a simulation. However, the rotational degrees of freedom are retained because the slow rotational relaxation of the polymer is important in polymer physics. In contrast, for heteropolymer biomolecule systems, both the translational and rotational degrees of freedom are removed from the sampled conformations of a biomolecule to allow for investigation of the structural fluctuations around its average conformation. In our previous report²⁵, we explained how to treat such sampled conformations with RMA, and succeeded in applying RMA to a heteropolymer system. Moreover, we demonstrated the effectiveness of RMA to investigate the transitions between some local minimum-energy states by calculating the free-energy surfaces for relaxation modes.

Although RMA is a powerful method for extracting slow modes, it requires a relatively high level of statistical precision of the time correlation matrices. Owing to this requirement, RMA requires a long simulation where many transitions between local minimum-energy states occur, which may not be a problem because such very long simulations have become feasible in recent years, as mentioned above. Moreover, RMA cannot handle a large number of degrees of freedom directly. Therefore, reduction of the degrees of freedom is necessary for application of RMA to protein systems. To achieve this,

we proposed a new analysis method, which is referred to as the principal component relaxation mode analysis (PCRMA) method. In this method, PCA is carried out first and then RMA is applied to a small number of principal components with large fluctuations. This method can systematically reduce the degrees of freedom. We also proposed the RMA method using multiple evolution times, which can reduce the contribution of the fast modes efficiently. In our previous report²⁶, we explained the combination of two proposed methods involving the PCRMA method using multiple evolution times, and demonstrated its applicability to an all-atom MD simulation of human lysozyme in aqueous solution.

Recently, methods to analyze the dynamics and kinetics of protein simulations have been developed. In particular, the Markov state model has been developed (see Refs. 28–33 and reviews^{34–36} and references cited therein) and used for many protein systems. The Markov state model can analyze transitions between local minimum-energy states, which are identified from clustering analysis methods. This is a powerful method for analyzing dynamics in the context of both long and short simulations of proteins. As mentioned above, in RMA, the relaxation modes and rates are given as left eigenfunctions and eigenvalues of the time-evolution operator of the master equation of the system, respectively^{11–13} (see Appendix A). From this point of view, RMA is related to Markov state models (see IID, Appendices A and B, and Ref. 38).

An analysis method of protein dynamics based on MD simulation was proposed³⁷ that separates linearly superimposed statistically independent signals by using time correlation functions, and was thus designated as time-structure based independent component analysis (tICA). The method is closely related to RMA, in that it determines statistically independent modes by solving the generalized eigenvalue problem with $t_0 = 0$. Recently, the combination method of tICA and a Markov state model was also proposed^{38,39}. In Ref. 38, a Markov state model was constructed from clustering in the subspace determined by tICA, which was calculated using a method similar to PCRMA.

In this study, we applied PCA and RMA to analyze the folding trajectories of a peptide, chignolin, near its folding transition temperature. As mentioned above, PCA cannot extract order parameters to easily identify the local minimum-energy states for a system with large conformational changes. This is because PCA extracts the modes with large structural fluctuations around an average structure, and the PC modes with large structural fluctuations do not correspond to the transitions between the local minimum-energy states. On the other hand, RMA can extract slow relaxation modes. The local minimum-energy states are usually stable and the system thus remains in this state for a long time during a simulation. The order parameters with slow relaxation may correspond to the directions between local minimum-energy states. Thus, slow relaxation modes may be suitable or-

der parameters to identify local minimum-energy states and the transitions between them.

To test this model, we performed a simulation of chignolin near its transition temperature. Chignolin consists of a 10 amino-acid polypeptide that adopts a β -hairpin turn structure, and is the smallest artificial protein⁴⁰, which has been used for testing new simulation algorithms. Indeed, there are many simulations for chignolin reported to date^{41–45}. Previous research has shown that chignolin has a stable state (native structure) and a misfolded state. The native and misfolded structures are hairpin-like structures (see Fig. 9). They have a common turn structure from Asp3 to Glu5 and have slightly different hydrogen bond patterns. Furthermore, the stability of the two states, i.e., how often these two states are observed during a simulation, has been found to depend on the force field⁴⁴. We considered that by increasing temperature, many transitions between the two states may occur within a several hundred-nanosecond simulation. Thus, we performed the simulation near the protein's transition temperature, which corresponds to a long simulation at room temperature. For estimation of the transition temperature, we refer to the results at a pressure of 1 atm obtained by the simulations in Ref. 45. We calculated the free-energy surfaces of the coordinates of PCA and RMA and show the effectiveness of RMA for extracting order parameters of the protein system with large conformational changes.

We also explain the relationship between RMA and Markov state models and propose a new analysis method called Markov state relaxation mode analysis (MSRMA). We evaluate the relaxation times of the states, which are defined by the free-energy surface from RMA, using a simple Markov state model and the new MSRMA method.

II. METHODS

A. Principal component analysis

PCA is a well-known method for analyzing the static properties of protein structural fluctuations obtained in a protein simulation system^{4–10}.

We now consider a biopolymer composed of N atoms. We assume that \mathbf{R} is a $3N$ -dimensional column vector that consists of a set of coordinates of atoms relative to their average coordinates. Namely,

$$\mathbf{R}^T = (\mathbf{r}'_1{}^T, \mathbf{r}'_2{}^T, \dots, \mathbf{r}'_N{}^T) = (x'_1, y'_1, z'_1, \dots, x'_N, y'_N, z'_N) \quad (2)$$

with

$$\mathbf{r}'_i = \mathbf{r}_i - \langle \mathbf{r}_i \rangle, \quad (3)$$

where \mathbf{r}_i is the coordinate of the i th atom of the biopolymer and $\langle \mathbf{r}_i \rangle$ is its average coordinate.

In PCA, the eigenvalue problem is solved as

$$C\mathbf{F}_n = \Lambda_n\mathbf{F}_n \quad \text{with} \quad \mathbf{F}_m^T\mathbf{F}_n = \delta_{m,n}. \quad (4)$$

Here, $C = \langle \mathbf{R}\mathbf{R}^T \rangle$ is the $3N \times 3N$ variance-covariance matrix: $C = (C_{i,j})$ with $C_{i,j} = \langle R_i R_j \rangle$. We now set the indices of the eigenvalues so that the relation $\Lambda_1 \geq \Lambda_2 \geq \dots \geq \Lambda_{3N}$ holds. The eigenvector \mathbf{F}_n with the eigenvalue Λ_n is referred to as the n th principal component axis. Note that $\Lambda_{3N-5} = \Lambda_{3N-4} = \dots = \Lambda_{3N} = 0$ because the translational and rotational degrees of freedom are removed. The coordinate \mathbf{R} can be expanded in terms of the PCA eigenvectors:

$$\mathbf{R} = \sum_{n=1}^{3N-6} \Phi_n \mathbf{F}_n \quad \text{with} \quad \Phi_n = \mathbf{F}_n^T \mathbf{R}. \quad (5)$$

Here, Φ_n is called the n th principal component. The variance of Φ_n is given by Λ_n .

B. Relaxation mode analysis

The RMA method was developed to identify slow motions in random spin systems and homopolymer systems. In RMA, we consider the following physical quantities:

$$\langle \phi_n(t)\phi_m(0) \rangle = \delta_{n,m} e^{-\lambda_n t}, \quad (6)$$

where ϕ_n and λ_n are the relaxation mode and its relaxation rate, respectively. Here, $\langle A(t)B(0) \rangle$ denotes the equilibrium time correlation function of physical quantity A at time t and B at time 0.

In the following, we briefly explain how to use RMA to extract slow relaxation modes and their relaxation rates from an MD simulation that satisfies the detailed balance condition. Here, we are only dealing with position coordinates because the relaxation of velocities (on a picosecond time scale) is usually faster than that of slow collective modes for coordinates (on a nanosecond time scale). In this case, the calculation process is the same as that for Monte Carlo simulations (see Ref. 25). Note that we describe the theoretical background of RMA in Appendix A and the application of the RMA method for an MD simulation in detail in Appendix B.

We use the following function as an approximate relaxation mode:

$$X_p = \mathbf{f}_p^T e^{-\Gamma^\dagger t_0/2} \mathbf{R} \quad (7)$$

Here, \mathbf{R} is given by Eq. (5) and Γ is the time-evolution operator of the master equation of the system (see Appendices A and B). The operator $e^{-\Gamma^\dagger t_0/2}$ is used to reduce the contributions of faster modes in \mathbf{R} , and the trial function becomes a better approximation as t_0 becomes larger²⁵. Note that Eq. (7) is the same as Eq. (30) of Ref. 25. X_p is a trial function, which is constructed as a linear combination of the expectation value of \mathbf{R} after a period $t_0/2$.

For the trial functions, the variational problem is equivalent to a generalized eigenvalue problem

$$C(t_0 + \tau)\mathbf{f}_p = e^{-\lambda_p \tau} C(t_0)\mathbf{f}_p, \quad (8)$$

where λ_p is the relaxation rate corresponding to X_p . The matrix $C(t)$ is defined by

$$C(t) = \langle \mathbf{R}(t) \mathbf{R}^T(0) \rangle. \quad (9)$$

The orthonormal condition for X_p is written as

$$\mathbf{f}_p^T C(t_0) \mathbf{f}_q = \delta_{p,q}. \quad (10)$$

Note that the number of meaningful relaxation modes is $3N - 6$ because the translational and rotational degrees of freedom are removed²⁵.

The time correlation functions of the approximate relaxation modes obtained can thus be written as

$$\langle X_p(t) X_q(0) \rangle \simeq \delta_{p,q} e^{-\lambda_p t}. \quad (11)$$

This relation holds exactly for $t = 0$ and $t = \tau$ and is expected to hold approximately for other values of $t \geq 0$.

From the orthonormal condition, the inverse transformation is derived as

$$e^{-\Gamma^\dagger t_0/2} \mathbf{R} = \sum_{p=1}^{3N-6} \mathbf{g}_p X_p, \quad (12)$$

where

$$\mathbf{g}_p = C(t_0) \mathbf{f}_p. \quad (13)$$

The time correlation functions of \mathbf{R} are given as

$$\begin{aligned} C(t) &= \langle \mathbf{R}(t) \mathbf{R}^T(0) \rangle \\ &= \sum_{p=1}^{3N-6} \sum_{q=1}^{3N-6} \mathbf{g}_p \mathbf{g}_q^T \langle X_p(t - t_0) X_q(0) \rangle \\ &\simeq \sum_{p=1}^{3N-6} \mathbf{g}_p \mathbf{g}_p^T e^{-\lambda_p(t-t_0)} \\ &= \sum_{p=1}^{3N-6} \tilde{\mathbf{g}}_p \tilde{\mathbf{g}}_p^T e^{-\lambda_p t} \end{aligned} \quad (14)$$

for $t \geq t_0$. Here,

$$\tilde{\mathbf{g}}_p = e^{\lambda_p t_0/2} \mathbf{g}_p. \quad (15)$$

Equations (11) and (14) lead to the relaxation mode expansion of \mathbf{R} :

$$\mathbf{R} \simeq \sum_{p=1}^{3N-6} \tilde{\mathbf{g}}_p X_p. \quad (16)$$

Because we are dealing with position coordinates only, $C(t)$ is a symmetric matrix owing to the detailed balance condition²⁷, and if t_0 is sufficiently large, the relaxation rates λ_p are real and positive, which correspond to pure relaxation. Then, we set the indices of λ_p so that $0 < \lambda_1 \leq \lambda_2 \leq \dots$ holds. On the basis of the approximate relaxation modes and rates, the correlation matrix

$C(t)$ with $t \geq t_0$ can be calculated. The accuracy of the present estimation of the relaxation modes and rates can be examined through comparison of the correlation matrices $C(t)$ calculated by the present method with those estimated directly by other means. In general, the time-displaced autocorrelations $C_{i,i}(t)$ are compared to check the obtained relaxation modes and rates.

C. Calculation of the free-energy surface

In PCA, from the probability density $P(\Phi_p, \Phi_q)$ of Φ_p and Φ_q , the dimensionless free energy, which is the free energy divided by $k_B T$, along the p th and q th principal component axes is calculated as

$$F(\Phi_p, \Phi_q) = -\ln P(\Phi_p, \Phi_q). \quad (17)$$

Here, k_B and T denote the Boltzmann constant and the temperature of the system, respectively. In the following, we abbreviate ‘‘dimensionless free energy’’ as ‘‘free energy’’ for simplicity. The indices p and q are usually set to numbers corresponding to large eigenvalues (e.g., $p = 1$ and $q = 2$).

In RMA, the quantity Y_p , corresponding to Φ_p in PCA, is defined by

$$Y_p = X_p |\tilde{\mathbf{g}}_p|. \quad (18)$$

Then, the free-energy surface as a function of Y_p and Y_q is calculated as

$$F(Y_p, Y_q) = -\ln P(Y_p, Y_q), \quad (19)$$

where $P(Y_p, Y_q)$ denotes the probability density of Y_p and Y_q . Here, X_p is calculated from \mathbf{R} as follows. Because of Eqs. (10) and (13), $\mathbf{f}_p^T \mathbf{g}_q = \delta_{p,q}$ holds, which leads to $\mathbf{f}_p^T \tilde{\mathbf{g}}_q = e^{\lambda_p t_0/2} \delta_{p,q}$. Therefore, by multiplying \mathbf{f}_p^T to both sides of Eq. (16), X_p is given as a function of \mathbf{R} as

$$X_p = \mathbf{f}_p^T \mathbf{R} \quad (20)$$

with

$$\tilde{\mathbf{f}}_p = e^{-\lambda_p t_0/2} \mathbf{f}_p. \quad (21)$$

D. Markov State Relaxation Mode Analysis

In this subsection, we consider the relation between RMA and Markov state models, and propose the new method of MSRMA. In the simplest Markov state model, the phase space of the system, where only the position coordinates are considered, is divided into clusters (subsets) S_i , $i = 1, \dots, n$. First, the joint probability $\bar{P}_{i,j}(\tau) = P(Q \in S_i, \tau; Q \in S_j, 0)$ that the state of the system Q is in the j th cluster at time 0 and is in the i th cluster at time $\tau > 0$ is calculated in a simulation. Second, the transition probability $\bar{T}_{i,j}(\tau)$ that the state of

the system is found in the i th cluster after time τ starting from a state in the j th cluster is calculated by

$$\bar{T}_{i,j}(\tau) = \bar{P}_{i,j}(\tau)/\bar{p}_j, \quad (22)$$

where $\bar{p}_j = P(Q \in S_j)$ is the probability that the state of the system is found in the j th cluster, which is estimated in the simulation. Then, by solving the eigenvalue problem

$$\bar{\mathbf{f}}_p^T \bar{T}(\tau) = \bar{\mathbf{f}}_p^T \bar{\Lambda}_p \quad (23)$$

for the transition matrix $\bar{T}(\tau) = (\bar{T}_{i,j}(\tau))$, the p th eigenvector $\bar{\mathbf{f}}_p$ and its eigenvalue $\bar{\Lambda}_p$ are obtained. The eigenvector $\bar{\mathbf{f}}_1 \propto (1, 1, \dots, 1)^T$ corresponds to the equilibrium state and its eigenvalue $\bar{\Lambda}_1 = 1$. Other eigenvectors $\bar{\mathbf{f}}_p$ represent structural transitions and the corresponding eigenvalues $\bar{\Lambda}_p$ give their relaxational timescales $\bar{\tau}_p$ as

$$\bar{\tau}_p = -\frac{\tau}{\ln \bar{\Lambda}_p}. \quad (24)$$

Note that in the Markov description, it is important that the states are defined in a kinetically meaningful way^{28,38}. We need to define the states that are classified by order parameters representing the dynamics and kinetics of the system. Even with a good choice of states, in order for a Markov description of the process to be accurate, the time interval τ should also be chosen carefully. In other words, for a Markov description to work, the time interval of the transition matrix τ must be chosen appropriately so that it is as large as the slowest relaxation time of the states. When plotting $\bar{\tau}_p$ as a function of τ , $\bar{\tau}_p$ slowly converges to the appropriate time scale when τ is increased. In addition, when a much longer τ than the slowest relaxation time of the states is used, the Markov state model is not expected to be accurate. Thus, we usually set the time interval τ to the value when the variation of $\bar{\tau}_p$ is sufficiently flat^{28,38}.

The above-mentioned procedure of the Markov state model is related to the following procedure of RMA. We call the following procedure the MSRMA. Similar to the description above in Section II B, we consider an approximate relaxation mode given by

$$\bar{X}_p = \bar{\mathbf{f}}_p^T e^{-\Gamma^\dagger t_0/2} \mathbf{\Delta}, \quad (25)$$

where $\mathbf{\Delta}$, as a function of the state Q of the system, is defined by

$$\mathbf{\Delta}(Q) = (\delta_1(Q), \delta_2(Q), \dots, \delta_n(Q))^T \quad (26)$$

with

$$\delta_i(Q) = \begin{cases} 1 & \text{for } Q \in S_i, \\ 0 & \text{for } Q \notin S_i. \end{cases} \quad (27)$$

The operator $e^{-\Gamma^\dagger t_0/2}$ reduces the contributions of faster modes in $\mathbf{\Delta}$. Then, the variational problem, which is equivalent to the eigenvalue problems (B1) and (B2) for

the conditional probability density $T_\tau(Q|Q')$ defined by (A13), leads to a generalized eigenvalue problem

$$\bar{C}(t_0 + \tau) \bar{\mathbf{f}}_p = e^{-\bar{\lambda}_p \tau} \bar{C}(t_0) \bar{\mathbf{f}}_p \quad (28)$$

or

$$\bar{\mathbf{f}}_p^T \bar{C}(t_0 + \tau) = e^{-\bar{\lambda}_p \tau} \bar{\mathbf{f}}_p^T \bar{C}(t_0) \quad (29)$$

with

$$\bar{\mathbf{f}}_p^T \bar{C}(t_0) \bar{\mathbf{f}}_q = \delta_{p,q}, \quad (30)$$

where

$$\bar{C}(t) = \langle \mathbf{\Delta}(t) \mathbf{\Delta}^T(0) \rangle. \quad (31)$$

Because $\bar{C}(t) = \bar{C}(t)^T$, Eqs. (28) and (29) are equivalent. It follows from the definition of $\mathbf{\Delta}$ that the (i, j) component of $\bar{C}(t)$ is the joint probability $\bar{P}_{i,j}(t)$: $\bar{C}(t) = (\bar{P}_{i,j}(t))$.

If we set $t_0 = 0$, the generalized eigenvalue problem (29) becomes the eigenvalue problem (23) with $\bar{\Lambda}_p = e^{-\bar{\lambda}_p \tau}$ or $\bar{\tau}_p = 1/\bar{\lambda}_p$, because $\bar{C}(0) = \text{diag}(\bar{p}_1, \dots, \bar{p}_n)$ and $\bar{C}(\tau) \bar{C}(0)^{-1} = \bar{T}(\tau)$. Thus, the Markov state model is a special case of MSRMA with $t_0 = 0$. Because the operator $e^{-\Gamma^\dagger t_0/2}$ in Eq. (25) reduces the contributions of faster modes in $\mathbf{\Delta}$, the solutions of the generalized eigenvalue problem (28) or (29) become better approximations to the slow relaxation modes and rates as t_0 becomes larger. Therefore, the relaxation times $\bar{\tau}_p$ obtained by the Markov state model are expected to be improved by solving Eqs. (28) or (29) with $t_0 > 0$ rather than Eq. (23).

III. COMPUTATIONAL DETAILS

An MD simulation was performed with the AMBER package (AMBER 11.0) with GPGPU using the ff99SB force field and TIP3P model⁴⁶. Chignolin consists of a 10-amino acid sequence: GYDPETGTWG. We generated an extended structure of chignolin using the leap command and solvated it with a 15 Å buffer of TIP3P water around the peptide in each direction. The numbers of atoms of chignolin and water molecules are 138 and 10,941 (3647 water molecules), respectively. Two potassium ions (Na^+) are included in the system, resulting in a net-neutral system. The total number of atoms in the system is 11,081. After energy minimization and heating, equilibration at a constant pressure (1 atm) and 450 K, a 50-ns MD simulation, was performed. Finally, a 750-ns MD simulation was performed following the equilibration at 1 atm and 450 K. We used a time step of 2 fs. The Langevin thermostat with a friction constant $\gamma = 2.0 \text{ ps}^{-1}$ was used for temperature control. The cutoff is 8 Å, which was used to limit the direct space sum for the Particle Mesh Ewald (PME) method of AMBER. For the equilibration and production run, pmemd with

GPGPU for MD simulations was used. For analysis, the coordinates were saved every 10 ps. The number of samples was 750,000.

We used the coordinates of C_α atoms on the backbone as coordinates, so that the degrees of freedom was 30. After removing the translational and rotational motions from the coordinates of C_α atoms^{47,48}, PCA and RMA were carried out on the coordinates of C_α atoms. For RMA, we set t_0 and τ to 10.0 ps and 20.0 ps, respectively.

IV. RESULTS AND DISCUSSION

A. Simulation Results

We performed a 750-ns MD simulation of chignolin in aqueous solution at 450 K. Before the present simulation, we performed two several- μ s simulations of chignolin at 300 K. In one simulation, chignolin folded to the native structure (see Fig. 9(a)) while in the other simulation, it folded to the misfolded structure (see Fig. 9(b)). After folding to the native or misfolded structures once, these structures were maintained, with few transitions between the structures, because the simulation times were not sufficiently long. To allow for large conformational changes between the structures to occur frequently and to be able to observe numerous transitions during a several hundred-ns simulation, we performed the simulation close to the transition temperature.

The time series of the RMSD of C_α atoms from the native structure is shown in Fig. 1. Here, the native structure is the first coordinate of 1UAO.pdb. RMSD is calculated after fitting the obtained structures to the native structure. Many transitions among the native-like structures (RMSD ≈ 1 Å), misfolded structures (RMSD ≈ 2 Å), and unfolded structures (RMSD ≈ 5 Å) occurred during the simulation.

This system is suitable for testing the effectiveness of RMA, because of the many transitions observed among structures, including with the completely unfolded structures. The present simulation conducted at 450 K corresponds to a long simulation conducted at 300 K, where many transitions are observed, similar to the observations in Ref. 1. We next analyzed the dynamics of chignolin in the system using PCA, RMA, and the newly proposed combined method MSRMA.

B. Results of principal component analysis

After a 750-ns production run was performed and the translational and rotational motions were removed from the coordinates of C_α atoms^{47,48}, we applied PCA to the system. The five largest eigenvalues obtained by PCA are listed in Table I. The p th eigenvalue is the variance of the p th principal component. The first PC mode mainly contributes to the global conformational fluctuation around the average structure. Figures 2(a) and 2(b) show the

free energy surfaces along the first and second PC axes (Φ_1 vs. Φ_2), and the second and third PC axes (Φ_2 vs. Φ_3), respectively, given by Eq. (17). We also show the free-energy surface of Φ_1 and Φ_3 in Fig. 2(c), because the two modes have a significantly slower relaxation than the others (see Fig. 4 and its discussion). The relations between RMSD from the native structure and PC components ((a) Φ_1 , (b) Φ_2 , or (c) Φ_3) are shown in Fig. 3. In Fig. 3(a), a local minimum-energy state can be observed near the value of $\Phi_1 \approx -4$. As the values of Φ_1 become large, the values of RMSD also become large. These results indicate that the direction of the first PC mode corresponds to the transition between the compact and unfolded structures. From the free-energy surface of Φ_1 and Φ_2 , we could not classify the native and misfolded states because the conformational difference between them is small compared with the conformational fluctuations of the system. As shown in Fig. 3(b), the direction of the second PC mode corresponds to a large fluctuation around slightly compact structures (RMSD ≈ 4), which does not correspond to the native and misfolded structures. Because of the two local minimum-energy states observed in Figs. 2(b) and 2(c) along the third PC axis, the direction of the third PC mode corresponds to the transition between two minimum states, which correspond to the native and misfolded states, even though there are many overlapping unfolded structures (see also Fig. 10). The free-energy surface of Φ_1 and Φ_3 can classify not only the native and misfolded states but also the unfolded state. It is suggested that it is more effective to use PC modes with slower relaxation rather than those with larger conformational fluctuations as the axes of the free-energy surface. However, PCA does not provide time information, and the native and misfolded states still show slight overlap on the free-energy surface of Φ_1 and Φ_3 (see Fig. 10(c) and its discussion).

Therefore, we next calculated the time-displaced autocorrelation functions of Φ_1 , Φ_2 , and Φ_3 , which are shown in Fig. 4. The first and third PC modes (in red and blue, respectively) show slow relaxation, while the second PC mode (in green) shows relatively faster relaxation. The second PC mode corresponds to large fluctuation of the slightly compact structures (RMSD ≈ 4), which are not completely compact like the native structure. Therefore, PCA could extract the large conformational fluctuation around the slightly compact structure as the second PC mode, even though its relaxation is faster.

C. Results of relaxation mode analysis

We applied RMA to the same coordinate data analyzed with PCA described above. In Supplemental Figure S1⁴⁹, the time-displaced autocorrelation functions of the x , y , z -coordinates for the i th C_α atom obtained by the simulation directly and reproduced by RMA from Eq. (14) are compared. These functions showed good agreement overall. This means that the appropriate relaxation modes

TABLE I. The eigenvalues Λ_p of the first to fifth PC modes, and their relaxation times $\tau_p (= 1/\Lambda_p)$ and conformational fluctuations \tilde{g}_p^2 of the first to fifth slowest relaxation modes.

p	PCA	RMA	
	Λ_p (\AA^2)	τ_p (ps)	\tilde{g}_p^2 (\AA^2)
1	20.17	3.7×10^3	6.93
2	7.01	2.4×10^3	10.81
3	4.53	1.5×10^3	1.85
4	2.58	7.5×10^2	2.87
5	1.60	6.4×10^2	1.74

and times were obtained.

Table I shows the relaxation times and conformational fluctuations of the five slowest relaxation modes (RMs). The three slowest relaxation modes were slower than the other modes. The second slowest relaxation mode showed the largest conformational fluctuation. Figure 5(a) and 5(b) show the free-energy surfaces along the first and second slowest RM axes (Y_1 vs. Y_2) and the second and third slowest RM axes (Y_2 vs. Y_3), respectively. In Fig. 6, the relations between the RMSD from the native structure and RM components (Y_1 (a), Y_2 (b), or Y_3 (c)) are shown. In Fig. 5(a), there are four characteristic regions. Two of them correspond to the local minimum-energy states of the native and misfolded structures. Random structures are located at the larger values of Y_2 and Y_3 . There is a free-energy minimum near the origin of Fig. 5(a). We refer to the state of the minimum as the intermediate state. Figures 5(a) and 6(a) indicate that the direction of the first RM corresponds to the transition between the native and misfolded states. Figures 5(a) and 6(b) indicate that the direction of the second RM corresponds to the transition between the misfolded state and the intermediate state. Furthermore, Figs. 5(b) and 6(c) suggest that the direction of the third RM may correspond to the transition between compact structures and the unfolded state.

Note that the normalized $\{\mathbf{g}_p\}$ are not orthogonal to each other, in contrast to $\{\mathbf{F}_p\}$. However, if the local minimum-energy states tend to be located in parallel along the slow RM axis, the direction of the axis corresponds to that for the transition between local minimum-energy states. In the previous work of Ref. 25, low free-energy paths, which connect to local minimum-energy states, were observed along the slow RM axes. The same tendency was observed in the present study. Fig. 7 shows the time-displaced autocorrelation functions of the p th RM component Y_p . The relaxation of $\langle Y_p(t)Y_p(0) \rangle$ becomes gradually faster as p becomes larger. Therefore, we succeeded in obtaining the order parameters with slow relaxation.

The suitable order parameters to identify the native and misfolded structures in the chignolin system have been identified in previous work, as follows: the distance between the amide nitrogen atom of Asp3 (Asp3N) and

the carbonyl oxygen atom of Gly7 (Gly7O), D(Asp3N-Gly7O), and that between Asp3N and the carbonyl oxygen atom of Thr8 (Thr8O), D(Asp3N-Thr8O)⁴¹. These order parameters could clearly distinguish between the native and misfolded states. Fig. 8 shows the free-energy surface along D(Asp3N-Gly7O) and D(Asp3N-Thr8O) obtained by the present simulation. The shape of the free-energy surface is similar to that obtained by Refs. 41 and 43. Although these order parameters are powerful for the system of chignolin, we generally need to search for good order parameters that will depend on the system. From RMA, we obtained good order parameters automatically not only to identify the local minimum-energy states but also to investigate the transitions between them.

In addition, we obtained interesting results for the intermediate state from RMA. The structures extracted for the four regions are listed in Table II, which correspond to the native, misfolded, intermediate, and unfolded states. The numbers of structures extracted for the native, misfolded, intermediate, and unfolded states are 24,824, 14,571, 5251, and 1806, respectively, and the total number of samples was 75,000. Fig. 9 shows movies of the structures in the four clusters (Multimedia view). We extracted every 100 structures for the native and misfolded states, every 20 structures for the intermediate state, and every 10 structures for the unfolded state to reduce the file size. Each movie shows only a set of structures and not a time sequence; thus, the order of the structures has no meaning. The native and misfolded structures appear as hairpin-like structures. The native state is stabilized by four hydrogen bonds: (a) between the oxygen atom of the side-chain carboxyl group of Asp3 (Asp3O $_{\delta}$) and the amide nitrogen atom of Thr6 (Thr6N), (b) between Asp3O $_{\delta}$ and the oxygen atom of the side-chain of Thr6 (Thr6O $_{\gamma}$), (c) between Asp3N and Thr8O, and (d) between the carbonyl oxygen atom of Gly1 (Gly1O) and the amide nitrogen atom of Gly10 (Gly10N). In addition, the side chains of Trp9 and Tyr2 are generally located on the same side. On the other hand, the misfolded state is stabilized by five hydrogen bonds: (a) between Asp3O $_{\delta}$ and Thr6N, (b) between Asp3O $_{\delta}$ and Thr6O $_{\gamma}$, (c) between the carbonyl oxygen atom of Asp3 (Asp3O) and the amide nitrogen atom of Gly7 (Gly7N), (d) between Asp3N and Gly7O, and (e) between Gly1O and the amide nitrogen atom of Gly9 (Gly9N). In addition, the side chains of Trp9 and Tyr2 are generally located on opposite sides. The terminal residues show large fluctuations. The misfolded state has different hydrogen bond patterns between Asp3N and Gly7O and between Gly1O and Gly9N. The obtained native and misfolded structures were similar to those obtained in previous studies^{41–43}.

In the intermediate state, chignolin tends to form a turn from Asp3 to Glu5, similar to the native and misfolded states. The intermediate state is stabilized by two hydrogen bonds: (a) between Asp3O $_{\delta}$ and Thr6N, and (b) between Asp3O $_{\delta}$ and Thr6O $_{\gamma}$. These hydrogen bonds

are also formed in the native and misfolded states. Table III shows the average RMSD values of residues from Asp3 to Glu5 and from Tyr2 to Trp9 for the four clusters. Here, we calculated the values using Visual Molecular Dynamics (VMD)⁵⁰. The average RMSD values of residues from Asp3 to Glu5 of the native, misfolded, and intermediate structures were all small. These results indicate that the intermediate state has the characteristic structure, i.e., the turn structure from Asp3 to Glu5.

In Fig. S2⁴⁹, we show the Ramachandran plots of each residue from Tyr2 to Trp9 for the four clusters. The plots of each residue from Tyr2 to Thr6 for the native and misfolded states are similar to each other. The difference of the backbone dihedral angles of Gly7 causes the different hydrogen bond patterns observed between the native and misfolded states. The plots of each residue from Asp3 to Glu5 for the intermediate state are similar to those for the native and misfolded states, indicating the formation of a turn structure. These results demonstrate that the native, misfolded, and intermediate structures have the same turn structure. The main difference between the unfolded state and the other states is in the distribution of the dihedral angles of Pro4, as shown in Fig. S2⁴⁹. This difference is responsible for the large RMSD value of residues from Asp3 to Glu5 of the unfolded state. Based on the structures of the four states obtained by RMA, we suggest that the dihedral angles are also good order parameters to classify the states in this system.

A previous report⁴² of a long simulation suggested that chignolin folds to the native or misfolded structures through the turn structure present in the intermediate state. The authors checked for the turn formation along their trajectories. Fig. S3⁴⁹ shows the RMSD values from the native structure for the four states defined in Table III as a function of time. We observed the intermediate state in transition not only between the native and unfolded states but also between the native and misfolded states. Therefore, the slow modes extracted by RMA clarify the conformational transitions in the folding and unfolding processes.

Fig. 10 shows the distributions for the native, misfolded, and intermediate states classified on the free-energy surfaces obtained from RMA in the planes of (a) Φ_1 and Φ_2 , (b) Φ_2 and Φ_3 , and (c) Φ_1 and Φ_3 . Although the free energy of Φ_1 and Φ_2 cannot distinguish between the native and misfolded states, that of Φ_2 and Φ_3 could. As shown in Fig. 10(c), there are still overlaps between the native and misfolded states. The structures in the intermediate state are distributed widely on the free-energy surface obtained by PCA and overlap on the areas of the folded and misfolded states corresponding to the free-energy surface of Φ_2 and Φ_3 . PCA could not identify the intermediate state, because the structural fluctuation near the terminal residues of the intermediate state is large and PCA extracts large structural fluctuations. RMA could extract the characteristic structure, i.e., the turn structure from Asp3 to Glu5, because the large fluctuations of the terminal residues have fast relaxation, and

RMA neglects the faster conformational changes.

These results strongly support the utility in clustering structures using the free energy obtained from RMA. We next investigated the transitions between the four clusters in detail. Fig. 11(a) shows the free energy surface of Y_1 and Y_2 with more contour lines. The free energy differences between the intermediate and the other three states are shown schematically in Fig. 11(b). The free energy difference from the intermediate state to the unfolded state was calculated to be approximately 2.1 kcal/mol. The free energy barrier seems to be small from the unfolded state to the transition state between the unfolded and intermediate states. Furthermore, given that the free energy difference from the intermediate state to the transition state toward the native state (0.5 kcal/mol) is lower than that toward the misfolded state (0.9 kcal/mol), the transition from the intermediate state to the native state appears to be easier than that to the misfolded state. These results suggest that the main folding path of chignolin from the unfolded to the native states passes through the intermediate state. The free energy difference from the native or misfolded states to their transition states toward the intermediate state were both high (2.2 or 2.0 kcal/mol, respectively). One reason could be that the hydrogen bonds between backbone atoms need to be broken in order to change from the native or misfolded states to the intermediate state. The slowest relaxation process is mostly related to the transition between the native and misfolded states; it corresponds to escape from the native state and the misfolded state to intermediate states. The second slowest relaxation process seems to be related to the transition between misfolded and unfolded states; it corresponds to escape from the misfolded state to the intermediate state and from the intermediate state to the unfolded state.

D. Results of Markov state relaxation mode analysis

Recently, Markov state models have been constructed in the discrete state space defined by the clustering in subspace determined by tICA^{38,39}. In the present work, we classified the structures into a smaller number of states by using the free-energy surface obtained by RMA, and then applied the Markov state model and MSRMA to analyze the states.

We divided the free-energy surface of Y_1 and Y_2 to the four regions shown in Fig. 11(a), and classified the structures into the following four states: native (S_1), misfolded (S_2), intermediate (S_3), and unfolded (S_4) states. After calculating the trajectories of δ_i ($i = 1, \dots, 4$), we solved the generalized eigenvalue problem of Eq. (28). Because $\bar{C}(t)$ is a symmetric matrix, $\bar{C}(t) = \bar{C}(t)^T$, we used $\frac{1}{2}(\bar{C}(t) + \bar{C}(t)^T)$ instead of $\bar{C}(t)$.

Fig. 12 shows the relaxation times $\bar{\tau}_p = 1/\bar{\lambda}_p$ obtained by MSRMA as a function of τ when $t_0 = 0, 10, 50, 100, 200$, and 500 ps. Because the first eigenvector \mathbf{f}_1 , pro-

portional to $(1, 1, 1, 1)^T$, corresponds to the steady state with infinite relaxation time $\tau_1 = \infty$, we show the second (a), third (b), and fourth (c) longest relaxation times in Fig. 12. The lines of $t_0 = 0$ correspond to the results of a simple Markov state model. In the case of $t_0 = 0$, $\bar{\tau}_p$ ($p = 2, 3$, and 4) values slowly approach the appropriate time scale, i.e., the values for plateau regions or peak values of the solid lines of Fig. 12, when τ is increased. Using the method for determining the value of τ described in Section IID, the appropriate time interval for τ was determined to be around 3 ns, which corresponds to the time scale of the slower relaxation times obtained by RMA. The relaxation times at $\tau = 3$ ns for the second, third, and fourth slowest relaxation modes were approximately 5, 3, and 1.8 ns, respectively, which are close to but slightly higher than those obtained by RMA at 3.7, 2.4, and 1.7 ns, respectively.

For the lines of $t_0 > 0$, the values of $\bar{\tau}_p$ quickly approach the appropriate time scale; i.e., those corresponding to the values for plateau regions or peak values of Fig. 12. Therefore, the slow relaxation times can be improved when applying MSRMA with $t_0 > 0$, which is introduced in order to reduce the relative weight of the faster modes contained in the physical quantities given by Eq. (25). The relaxation times are improved even if t_0 is small; in particular, the appropriate relaxation times are obtained using a shorter value for the time interval τ . The estimated relaxation times were approximately 5.5 ns, 3.5 ns, and 2.0 ns (using $t_0 = 0.2$ ns and $\tau = 1$ ns).

The normalized time-displaced autocorrelation functions of Δ both calculated directly and reproduced by MSRMA using Eq. (14) are shown in Fig. 13. The function is given by

$$\begin{aligned} \hat{C}_{i,i}(t) &= \frac{\langle (\delta_i(t) - \langle \delta_i(t) \rangle) (\delta_i(0) - \langle \delta_i(0) \rangle) \rangle}{\langle (\delta_i(0) - \langle \delta_i(0) \rangle)^2 \rangle} \\ &= \frac{\langle \delta_i(t) \delta_i(0) \rangle - \bar{p}(i)^2}{\bar{p}(i) - \bar{p}(i)^2}. \end{aligned} \quad (32)$$

Note that, in the present case, the summation in Eq. (14) is taken from $p = 1$ to 4. The results obtained directly shown in Fig. 13 indicate that the time-displaced autocorrelation functions of $i = 1$ and 2, which correspond to the native and misfolded states, respectively, have similar slower relaxations. The time-displaced autocorrelation function of $i = 3$ and 4, which correspond to the intermediate and unfolded states, respectively, have similar relaxations, which are slightly faster compared to those of $i = 1$ and 2.

The correlation matrix $\bar{C}(t)$ reproduced by Eq. (14) must be equal to that directly calculated by the simulation at $t = t_0$ and $t = t_0 + \tau$, because Eq. (11) holds exactly for $t = 0$ and $t = \tau$, as mentioned above in Section IIB. Therefore, as shown in Fig. 13, all lines of $\hat{C}_{i,i}(t)$ reproduced by Eq. (14) go through the points of directly calculated $\hat{C}_{i,i}(t)$ at $t = t_0$ and $t = t_0 + \tau$. In the case of $t_0 = 0$ ps and $\tau = 1000$ ps, shown in Fig. 13 (a), reproduced $\hat{C}_{i,i}(t)$ is larger than the directly calculated

$\hat{C}_{i,i}(t)$ for $t_0 = 0 < t < t_0 + \tau = \tau$, and is smaller for $t_0 + \tau = \tau < t$. As a result, the relaxation times obtained by MSRMA are underestimated. This is due to the above-mentioned restriction and the existence of fast relaxation modes in the directly calculated $\hat{C}_{i,i}(t)$, which causes the fast initial decay of $\hat{C}_{i,i}(t)$. These fast relaxation modes cannot be described by the three relaxation modes used in MSRMA. Thus, the results of MSRMA with $t_0 = 0$ are improved by using a longer τ as shown in Fig. 13(b), which is the usual method for the simple Markov state model. Comparison of the results of MSRMA for $t_0 = 10$ ps and $\tau = 1000$ ps shown in Fig. 13(c) with those for $t_0 = 0$ ps and $\tau = 1000$ ps shown in Fig. 13(a), and comparison of those for $t_0 = 10$ ps and $\tau = 3000$ ps shown in Fig. 13(d) with those for $t_0 = 0$ ps and $\tau = 3000$ ps shown in Fig. 13(b) make it clear that the results of MSRMA are improved by using finite t_0 , even if t_0 is small. Fig. 12 clearly shows that the relaxation times obtained for $t_0 = 10$ ps and $\tau = 1000$ ps are similar to those obtained for $t_0 = 0$ ps and $\tau = 3000$ ps. The results for $t_0 = 200$ ps and $\tau = 100$ ps shown in Fig. 13(e) and those for $t_0 = 500$ ps and $\tau = 100$ ps shown in Fig. 13(f) demonstrate that a good description of the relaxation of the states can be obtained by using MSRMA with finite t_0 , even if τ is small. Note that the values of t_0 and $t_0 + \tau$ [200 ps and 300 ps for Fig. 13(e), and 500 ps and 600 ps for Fig. 13(e)] are much smaller than the value of τ (3000 ps) used to estimate the relaxation times by MSRMA with $t_0 = 0$, i.e., the simple Markov state model.

TABLE II. The definitions of four clusters: native state (Native), misfolded state (Misfolded), intermediate state (Intermediate), and unfolded state (Unfolded). The total number of samples in the four regions is 46,452, and the total number of samples overall is 75,000. The structures in the ranges from min to max of Y_1 and Y_2 (for native, misfolded, and intermediate states) or Y_2 and Y_3 (for unfolded state) were extracted.

Cluster	Native	Misfolded	Intermediate	Unfolded
	<i>min: max</i>	<i>min: max</i>	<i>min: max</i>	<i>min: max</i>
Y_1	-4.3:-1.8	1.2:4.2	1.2:3.7	
Y_2	-2.0:1.0	-6.5:-2.5	1.5:4.0	5.0:16.0
Y_3				4.0:10.0
No. of samples	24824	14571	5251	1806

V. CONCLUSIONS

In this study, we applied RMA to extract reaction coordinates for a protein system characterized by large conformational changes such as folding/unfolding simulation. We performed a 750-ns simulation of chignolin near its transition temperature and observed many

TABLE III. The average RMSD values (\AA) for the four clusters. The structures in all clusters were fit to the first structure in the native state using backbone atoms from Asp3 to Glu5. Then, the average RMSD from the average structure of each cluster was calculated for the backbone atoms from Tyr2 to Trp9 or from Asp3 to Glu5.

	Tyr2 to Trp9	Asp3 to Glu5
Native	1.198	0.185
Misfolded	1.652	0.212
Intermediate	3.671	0.245
Unfolded	8.406	0.993

transitions between the most stable, misfolded, and unfolded states. RMA could extract the slow relaxation modes. The local minimum-energy states were usually stable and the system remained in this state for a long time during the simulation. The order parameters with slow relaxation corresponded to the directions between the local minimum-energy states. Therefore, these slow relaxation modes indicate the suitable order parameters for identifying the local minimum-energy states automatically. From the free-energy surfaces obtained by RMA, we identified not only the native and misfolded states but also the intermediate state. RMA neglected the conformational changes with fast relaxation and extracted the intermediate state showing a turn structure from Asp3 to Glu5. Thus, using RMA clarified the folding process of chignolin to the native or misfolded structures through the turn structure. Analysis of the free energy differences further revealed that the transition from the folding to native state through the turn structure is easier than that to the misfolded state.

Note that in simulations, the free-energy surface depends on both the temperature and simulation time in practice. In general, it is still difficult to determine whether or not a simulation time is sufficient. The free-energy surface obtained in the present study resulted from a 750-ns simulation near the transition temperature. To support the validity of the free-energy surface, we also need to investigate the stability of the local minimum-energy states. In addition, the free-energy surface near a transition temperature is different from that at a room temperature. Nevertheless, understanding the dynamics and kinetics of chignolin near its transition temperature can provide important information on the folding process. Overall, these results indicated that RMA can be used to effectively analyze long simulations at room temperature and is also useful for investigating systems with large conformational changes, such as intrinsically disordered proteins and protein folding.

Our experience of RMA suggests that a simulation time longer than approximately $10 \tau_{\text{slow}}$ is preferable, where τ_{slow} is the slowest relaxation time. In addition, even if such a long simulation cannot be performed, rare transitions, (e.g., one transition), can be obtained during the simulation to identify local minimum-energy states

and the transitions between them.

We have here proposed a new analysis method called MSRMA. By applying RMA to the Markov state model, we introduced the evolution time t_0 , which reduced the relative weight of the faster modes contained in the physical quantities. From clustering the states using the free-energy surface obtained by RMA, we constructed a Markov state model and performed MSRMA. Analysis and comparison of the relaxation times of the states obtained by a simple Markov state model and MSRMA showed similar relaxation times to those obtained from RMA. Moreover, we show that MSRMA clearly improves the approximate relaxation times.

ACKNOWLEDGMENTS

This work was supported, in part, by the Grant-in-Aid for Scientific Research on Innovative Areas ‘‘Material Design through Computics’’ from the Ministry of Education, Culture, Sports, Science and Technology (MEXT), Japan. This research is partially supported by Initiative on Promotion of Supercomputing for Young or Women Researchers, Supercomputing Division, Information Technology Center, The University of Tokyo, and HA-PACS at the CCS, University of Tsukuba.

Appendix A: Relaxation modes

We consider a Langevin equation for a biomolecule with N atoms:

$$m_i \frac{d\mathbf{v}_i}{dt} = -\zeta \mathbf{v}_i - \frac{\partial}{\partial \mathbf{r}_i} U(\{\mathbf{r}_j\}) + \mathbf{w}_i \quad (\text{A1})$$

with

$$\frac{d\mathbf{r}_i}{dt} = \mathbf{v}_i. \quad (\text{A2})$$

Here, $\mathbf{r}_i(t)$ and $\mathbf{v}_i(t)$ denote the position and the velocity of the i th atom at time t , respectively. m_i is the mass of the i th atom and ζ is the friction constant. The interaction between atoms is described by the potential $U(\{\mathbf{r}_i\}) = U(\mathbf{r}_1, \dots, \mathbf{r}_N)$. The random force $\mathbf{w}_i(t)$ acting on the i th atom is a Gaussian white stochastic process and satisfies

$$\langle w_{i,\alpha}(t) w_{j,\beta}(t') \rangle = 2\zeta k_B T \delta_{\alpha,\beta} \delta_{i,j} \delta(t - t'), \quad (\text{A3})$$

where $w_{i,\alpha}$, k_B , and T denote the α -component of \mathbf{w}_i ($\alpha = x, y, \text{ or } z$), the Boltzmann constant, and the temperature of the system, respectively. The Kramers equation equivalent to Eqs. (A1) and (A2) can be written as

$$\frac{\partial}{\partial t} P(Q, t) = -\Gamma(Q) P(Q, t). \quad (\text{A4})$$

Here, $Q = \{\mathbf{r}_1, \dots, \mathbf{r}_N, \mathbf{v}_1, \dots, \mathbf{v}_N\}$ denotes a point in the phase space of the system, and $P(Q, t)dQ$ denotes the

probability that the system is found at time t in an infinitesimal volume dQ at the point Q in the phase space. The time-evolution operator Γ is explicitly given by

$$\Gamma(Q) = \sum_{i=1}^N \left\{ \frac{\partial}{\partial \mathbf{r}_i} \cdot \mathbf{v}_i - \frac{1}{m_i} \frac{\partial}{\partial \mathbf{v}_i} \cdot \frac{\partial U}{\partial \mathbf{r}_i} - \frac{\zeta}{m_i} \frac{\partial}{\partial \mathbf{v}_i} \cdot \left(\mathbf{v}_i + \frac{k_B T}{m_i} \frac{\partial}{\partial \mathbf{v}_i} \right) \right\}. \quad (\text{A5})$$

Because Eqs. (A1) and (A2) are nonlinear for anharmonic potentials, it is generally difficult to define relaxation modes as normal coordinates of the equations. However, as explained below, we can define relaxation modes on the basis of Eq. (A4), which is a linear equation.

Let $\phi_n(Q)$ and $\psi_n(Q)$ denote the left and right eigenvectors of the time-evolution operator $\Gamma(Q)$ with an eigenvalue λ_n , respectively:

$$\Gamma(Q)\psi_n(Q) = \lambda_n\psi_n(Q) \quad (\text{A6})$$

and

$$\Gamma^\dagger(Q)\phi_n(Q) = \lambda_n\phi_n(Q). \quad (\text{A7})$$

Here, $\Gamma^\dagger(Q)$ is the adjoint operator of $\Gamma(Q)$ defined by

$$\int f(Q)(\Gamma(Q)g(Q))dQ = \int (\Gamma^\dagger(Q)f(Q))g(Q)dQ, \quad (\text{A8})$$

which satisfies

$$\Gamma(Q)\delta(Q - Q') = \Gamma^\dagger(Q')\delta(Q - Q'). \quad (\text{A9})$$

The eigenvectors are chosen to satisfy the orthonormal condition:

$$\int dQ \phi_n(Q)\psi_m(Q) = \delta_{n,m}. \quad (\text{A10})$$

The equilibrium distribution function for Kramers equation

$$P_{\text{eq}}(Q) \propto \exp \left[-\frac{1}{k_B T} \left\{ \frac{1}{2} \sum_i m_i \mathbf{v}_i^2 + U(\{\mathbf{r}_j\}) \right\} \right] \quad (\text{A11})$$

is a right eigenfunction of $\Gamma(Q)$ with zero eigenvalue: $\Gamma(Q)P_{\text{eq}}(Q) = 0$. The corresponding left eigenfunction is 1.

From Eq. (A4), a formal solution of $P(Q, t)$ for an initial condition $P(Q, 0) = P_0(Q)$ is given by

$$P(Q, t) = e^{-\Gamma(Q)t} P_0(Q). \quad (\text{A12})$$

The conditional probability $T_t(Q|Q')dQ$ that the system is found at time t in an infinitesimal volume dQ at Q , given that the system is at Q' at time 0, is then given by

$$T_t(Q|Q') = e^{-\Gamma(Q)t} \delta(Q - Q'). \quad (\text{A13})$$

The time-displaced correlation functions of two physical quantities $A(Q)$ and $B(Q)$ in the equilibrium are given

by

$$\begin{aligned} \langle A(t)B(0) \rangle &= \int \int A(Q)T_t(Q|Q')B(Q')P_{\text{eq}}(Q')dQdQ' \\ &= \int A(Q)e^{-\Gamma(Q)t}B(Q)P_{\text{eq}}(Q)dQ \\ &= \int \left\{ e^{-\Gamma^\dagger(Q)t}A(Q) \right\} B(Q)P_{\text{eq}}(Q)dQ \end{aligned} \quad (\text{A14})$$

We define a quantity $\hat{\phi}_n(Q)$ through

$$\psi_n(Q) = \hat{\phi}_n(Q)P_{\text{eq}}(Q). \quad (\text{A15})$$

From Eq. (A14), the equilibrium time-displaced correlation function of $\phi_n(Q)$ and $\hat{\phi}_m(Q)$ is given by

$$\langle \phi_n(t)\hat{\phi}_m(0) \rangle = \delta_{n,m}e^{-\lambda_n t}. \quad (\text{A16})$$

If two quantities $A(Q)$ and $B(Q)$ are expanded as

$$A(Q) = \sum_n a_n \phi_n(Q) \quad \text{and} \quad B(Q) = \sum_n \hat{b}_n \hat{\phi}_n(Q), \quad (\text{A17})$$

with

$$a_n = \int dQ A(Q)\hat{\phi}_n(Q)P_{\text{eq}}(Q) = \langle A\hat{\phi}_n \rangle \quad (\text{A18})$$

and

$$\hat{b}_n = \int dQ \phi_n(Q)B(Q)P_{\text{eq}}(Q) = \langle \phi_n B \rangle, \quad (\text{A19})$$

then the time correlation function of A and B in the equilibrium is given by

$$\langle A(t)B(0) \rangle = \sum_n a_n \hat{b}_n e^{-\lambda_n t}. \quad (\text{A20})$$

Thus, in terms of $\phi_n(Q)$ and $\hat{\phi}_n(Q)$, the correlation function $\langle A(t)B(0) \rangle$ is decomposed into a sum of exponentially relaxing contributions. Therefore, we use two sets of functions, $\{\phi_n(Q)\}$ and $\{\hat{\phi}_n(Q)\}$, as relaxation modes and call $\{\lambda_n\}$ their relaxation rates. Note that the eigenvalues λ_n are not necessarily real in general. Therefore, the terms $e^{-\lambda_n t}$ in Eq. (A20) can describe oscillatory behavior¹³.

The Kramers equation satisfies the detailed balance condition²⁷

$$P_{\text{eq}}(Q')\Gamma(Q)\delta(Q - Q') = P_{\text{eq}}(\epsilon Q)\Gamma^\dagger(\epsilon Q)\delta(\epsilon Q - \epsilon Q'), \quad (\text{A21})$$

and

$$P_{\text{eq}}(Q) = P_{\text{eq}}(\epsilon Q), \quad (\text{A22})$$

where ϵQ denotes the time-reversed state of the state Q , namely $\epsilon Q = \{\epsilon_1 \mathbf{r}_1, \dots, \epsilon_N \mathbf{r}_N, \epsilon_{N+1} \mathbf{v}_1, \dots, \epsilon_{2N} \mathbf{v}_N\}$ with

$$\epsilon_i = \begin{cases} 1 & \text{for } i = 1, \dots, N, \\ -1 & \text{for } i = N + 1, \dots, 2N. \end{cases} \quad (\text{A23})$$

This leads to the relation

$$\hat{\phi}_n(Q) \propto \phi_n(\epsilon Q) \quad (\text{A24})$$

between the relaxation modes.

Appendix B: Relaxation mode analysis

The eigenvalue problem of eqs. (A6) and (A7) can be written as

$$e^{-\Gamma(Q)\tau} \hat{\phi}_n(Q) P_{\text{eq}}(Q) = e^{-\lambda_n \tau} \hat{\phi}_n(Q) P_{\text{eq}}(Q) \quad (\text{B1})$$

and

$$e^{-\Gamma^\dagger(Q)\tau} \phi_n(Q) = e^{-\lambda_n \tau} \phi_n(Q). \quad (\text{B2})$$

This eigenvalue problem is equivalent to the variational problem

$$\delta \mathcal{R} = 0 \quad (\text{B3})$$

for

$$\delta \mathcal{R}[\phi_n, \hat{\phi}_n] = \frac{\langle \phi_n(\tau) \hat{\phi}_n(0) \rangle}{\langle \hat{\phi}_n \hat{\phi}_n \rangle} \quad (\text{B4})$$

and the stationary value of \mathcal{R} gives the eigenvalue $\exp(-\lambda_n \tau)$. In Ref. 13, a linear combination of relevant quantities is used as a trial function for ϕ_n and $\hat{\phi}_n$, and the variational problem is solved. The solution is given as a solution of a generalized eigenvalue problem for the equilibrium time-displaced correlation matrices of the quantities.

We use the following functions as an approximate relaxation mode:

$$X_p = \mathbf{f}_p^T e^{-\Gamma^\dagger t_0/2} \mathbf{R} \quad (\text{B5})$$

and

$$\hat{X}_p = P_{\text{eq}}^{-1} \hat{\mathbf{f}}_p^T e^{-\Gamma t_0/2} \mathbf{R} P_{\text{eq}} \quad (\text{B6})$$

as the p th trial functions for $\phi_n(Q)$ and $\hat{\phi}_n(Q)$, respectively, where

$$\mathbf{f}_p = (f_{p,1}, f_{p,2}, \dots, f_{p,6N})^T \quad (\text{B7})$$

and

$$\hat{\mathbf{f}}_p = (\hat{f}_{p,1}, \hat{f}_{p,2}, \dots, \hat{f}_{p,6N})^T \quad (\text{B8})$$

are variational parameters. Here, \mathbf{R} is defined by

$$\mathbf{R} = (\mathbf{r}'_1, \mathbf{r}'_2, \dots, \mathbf{r}'_N, \mathbf{v}'_1, \dots, \mathbf{v}'_N)^T \quad (\text{B9})$$

with

$$\mathbf{r}'_i = \mathbf{r}_i - \langle \mathbf{r}_i \rangle \quad \text{and} \quad \mathbf{v}'_i = \mathbf{v}_i - \langle \mathbf{v}_i \rangle, \quad (\text{B10})$$

where \mathbf{r}_i and \mathbf{v}_i are the coordinate and velocity vectors of the i th atom of the biopolymer, and $\langle \mathbf{r}_i \rangle$ and $\langle \mathbf{v}_i \rangle$ are the average coordinate and velocity vectors. The operators $e^{-\Gamma^\dagger t_0/2}$ and $e^{-\Gamma t_0/2}$ are used to reduce the contributions of faster modes in \mathbf{R} and $\mathbf{R} P_{\text{eq}}$, respectively, and the trial functions become better approximations as t_0 becomes larger.

For the trial functions Eqs. (B5) and (B6), the variational equation is equivalent to a generalized eigenvalue problem

$$\mathbf{f}_p^T C(t_0 + \tau) = e^{-\lambda_p \tau} \mathbf{f}_p^T C(t_0) \quad (\text{B11})$$

and

$$C(t_0 + \tau) \hat{\mathbf{f}}_p = e^{-\lambda_p \tau} C(t_0) \hat{\mathbf{f}}_p, \quad (\text{B12})$$

where λ_p is the relaxation rate corresponding to X_p and \hat{X}_p . The matrix $C(t)$ is an equilibrium time-displaced correlation matrix defined by

$$C(t) = \langle \mathbf{R}(t) \mathbf{R}^T(0) \rangle. \quad (\text{B13})$$

The orthonormal condition for X_p and \hat{X}_p is written as

$$\mathbf{f}_p^T C(t_0) \hat{\mathbf{f}}_q = \delta_{p,q}. \quad (\text{B14})$$

The time correlation functions of relaxation modes are now written as

$$\langle X_p(t) \hat{X}_q(0) \rangle \simeq \delta_{p,q} \exp(-\lambda_p t). \quad (\text{B15})$$

Because X_p and \hat{X}_q are approximate relaxation modes determined by solving for one value of τ , the relation holds exactly for $t = 0$ and $t = \tau$, and is expected to hold approximately for other values of $t \geq 0$.

By using Eq. (A24), we choose

$$\hat{X}_p(Q) = X_p(\epsilon Q). \quad (\text{B16})$$

Then, the detailed balance condition (A21) leads to

$$\hat{\mathbf{f}}_p = E \mathbf{f}_p \quad (\text{B17})$$

with

$$E = \text{diag}(\epsilon_1, \epsilon_1, \epsilon_1, \epsilon_2, \epsilon_2, \epsilon_2, \dots, \epsilon_{2N}, \epsilon_{2N}, \epsilon_{2N}). \quad (\text{B18})$$

Because the detailed balance condition also leads to

$$C(t)^T = E C(t) E, \quad (\text{B19})$$

it can be seen that the generalized eigenvalue problems (B11) and (B12) are equivalent.

From the orthonormal condition, the inverse transformation of Eqs. (B5) and (B6) is derived as

$$e^{-\Gamma^\dagger t_0/2} \mathbf{R} = \sum_{p=1}^{6N-12} \mathbf{g}_p X_p \quad (\text{B20})$$

and

$$P_{\text{eq}}^{-1} e^{-\Gamma t_0/2} \mathbf{R} P_{\text{eq}} = \sum_{p=1}^{6N-12} \hat{\mathbf{g}}_p \hat{X}_p \quad (\text{B21})$$

with

$$\mathbf{g}_p = C(t_0) \hat{\mathbf{f}}_p \quad \text{and} \quad \hat{\mathbf{g}}_p = C(t_0)^T \mathbf{f}_p. \quad (\text{B22})$$

In Eqs. (B20) and (B21), it is assumed that the translational and rotational motions are removed. It follows from Eqs. (B17) and (B19) that

$$\hat{\mathbf{g}}_p = E\mathbf{g}_p. \quad (\text{B23})$$

By using Eqs. (B20) and (B21), the equilibrium time-displaced correlation functions of \mathbf{R} are given as

$$\begin{aligned} C(t) = \langle \mathbf{R}(t)\mathbf{R}^T(0) \rangle &= \sum_{p=1}^{6N-12} \sum_{q=1}^{6N-12} \mathbf{g}_p \hat{\mathbf{g}}_q^T \langle X_p(t-t_0)X_q(0) \rangle \\ &\simeq \sum_{p=1}^{6N-12} \tilde{\mathbf{g}}_p \tilde{\mathbf{g}}_p^T e^{-\lambda_p t} \end{aligned} \quad (\text{B24})$$

for $t \geq t_0$. Here,

$$\tilde{\mathbf{g}}_p = e^{\lambda_p t_0/2} \mathbf{g}_p \quad \text{and} \quad \tilde{\hat{\mathbf{g}}}_p = e^{\lambda_p t_0/2} \hat{\mathbf{g}}_p. \quad (\text{B25})$$

Note that

$$\tilde{\hat{\mathbf{g}}}_p = E\tilde{\mathbf{g}}_p. \quad (\text{B26})$$

Equation (B24) can be regarded as Eq. (A20) with the mode expansion

$$\mathbf{R} \simeq \sum_{p=1}^{6N-12} \tilde{\mathbf{g}}_p X_p \quad \text{and} \quad \mathbf{R} \simeq \sum_{p=1}^{6N-12} \tilde{\hat{\mathbf{g}}}_p \hat{X}_p. \quad (\text{B27})$$

The RMA method explained above can be summarized as follows. The approximate relaxation modes X_p and \hat{X}_q , which are specified by \mathbf{f}_p and $\hat{\mathbf{f}}_p = E\mathbf{f}_p$ through Eqs. (B5) and (B6), and the corresponding relaxation rate λ_p are determined by solving the eigenvalue problem (B11) or (B12), which are equivalent, with the condition (B14), where the equilibrium time-displaced correlation matrix $C(t)$ is defined by (B13). In terms of the approximate relaxation modes and rates, $C(t)$ with $t \geq t_0$ can be calculated from Eq. (B24), where $\tilde{\mathbf{g}}_p$ and $\tilde{\hat{\mathbf{g}}}_p = E\tilde{\mathbf{g}}_p$ are given by Eq. (B25). By comparing $C(t)$ calculated in the manner described above with that directly calculated by simulations, the accuracy of the approximate relaxation modes and rates can be examined.

In this paper, we deal with position coordinates only, for which $\epsilon_i = 1$. Therefore, the following relations hold: $X_p = \hat{X}_p$, $\mathbf{f}_p = \hat{\mathbf{f}}_p$, $\mathbf{g}_p = \hat{\mathbf{g}}_p$, $\tilde{\mathbf{g}}_p = \tilde{\hat{\mathbf{g}}}_p$, and $C(t) = C(t)^T$.

¹K. Lindorff-Larsen, S. Piana, R. O. Dror, and D. E. Shaw, *Science* **334**, 517 (2011); R. O. Dror, R. M. Dirks, J. P. Grossman, H. Xu, and D. E. Shaw, *Annu. Rev. Biophys.* **41**, 429 (2012).

²T. J. Lane, D. Shukla, K. A. Beauchamp, and V. S. Pande, *Curr. Opin. Struct. Biol.* **23**, 58 (2013).

³P. L. Freddoline, C. B. Harrison, Y. Liu, and K. Schulten, *Nature Physics* **6**, 751 (2010).

⁴A. Kitao, F. Hirata, and N. Go, *Chem. Phys.*, **158**, 447–472 (1991).

⁵T. Ichiye and M. Karplus, *Proteins*, **11**, 205–217 (1991).

⁶R. Abagyan and P. Argos, *J. Mol. Biol.*, **225**, 519–532 (1992).

⁷A.E. Garcia, *Phys. Rev. Lett.*, **68**, 2696–2699 (1992).

⁸S. Hayward, A. Kitao, F. Hirata, and N. Go, *J. Mol. Biol.*, **234**, 1207–1217 (1993).

⁹A. Amadei, A.B.M. Linssen, and H.J.C. Berendsen, *Proteins* **17**, 412–425 (1993).

¹⁰R. M. Levy, A. R. Srinivasan, W. K. Olson, and J. A. McCammon, *Biopolymers*, **23**, 1099–1112 (1984).

¹¹H. Takano and S. Miyashita, *J. Phys. Soc. Jpn.*, **64**, 3688–3698 (1995).

¹²S. Koseki, H. Hirao, and H. Takano, *J. Phys. Soc. Jpn.*, **66**, 1631–1637 (1997).

¹³H. Hirao, S. Koseki, and H. Takano, *J. Phys. Soc. Jpn.*, **66**, 3399–3405 (1997).

¹⁴K. Hagita and H. Takano, *J. Phys. Soc. Jpn.*, **68**, 401–407 (1999).

¹⁵K. Hagita, S. Koseki and H. Takano, *J. Phys. Soc. Jpn.*, **68**, 2144–2145 (1999).

¹⁶K. Hagita, D. Ishizuka and H. Takano, *J. Phys. Soc. Jpn.*, **70**, 2897–2902 (2001).

¹⁷K. Hagita and H. Takano, *J. Phys. Soc. Jpn.*, **71**, 673–676 (2002).

¹⁸K. Hagita and H. Takano, *J. Phys. Soc. Jpn.*, **72**, 1824–1827 (2003) and references therein.

¹⁹S. Saka and H. Takano, *J. Phys. Soc. Jpn.*, **77**, 034001 (2008).

²⁰N. Iwaoka and H. Takano, *J. Phys. Soc. Jpn.*, **82**, 064801 (2013).

²¹N. Iwaoka and H. Takano, *J. Phys. Soc. Jpn.*, **83**, 123801 (2014).

²²N. Iwaoka, K. Hagira, and H. Takano, *J. Phys. Soc. Jpn.*, **84**, 044801 (2015).

²³P. G. de Gennes, *Scaling Concepts in Polymer Physics* (Cornell University Press, Ithaca, 1984).

²⁴M. Doi and S. F. Edwards, *The Theory of Polymer Dynamics* (Oxford University Press, Oxford, 1986).

²⁵A. Mitsutake, H. Iijima, and H. Takano, *J. Chem. Phys.*, **135**, 164102 (2011).

²⁶T. Nagai, A. Mitsutake, and H. Takano, *J. Phys. Soc. Jpn.*, **82**, 023803 (2013); T. Nagai, A. Mitsutake, and H. Takano, *Seibutsu Butsuri (Biophysics)*, **49**, Supplement S75, (Abstracts for the 47st annual meeting, The Biophysical Society of Japan) (2009).

²⁷H. Risken, *The Fokker-Planck Equation: Methods of Solution and Applications*, 2nd Ed. (Springer-Verlag, Berlin, 1989).

²⁸W.C. Swope, J.W. Pitera, and F. Suits, *J. Phys. Chem. B*, **108**, 6571 (2004).

²⁹N. Singhal, C. Snow, and V.S. Pande, *J. Chem. Phys.*, **121**, 415 (2004).

³⁰J.D. Chodera, W.C. Swope, J.W. Pitera, and K.A. Dill, *Multi-scale Model. Simul.* **5**, 1214 (2006).

³¹J.D. Chodera, K.A. Dill, N. Singhal, V.S. Vande, W.C. Swope, and J.W. Pitera, *J. Chem. Phys.* **126**, 155101 (2007).

³²F. Noé, U. Horenko, C. Schütte, and J.C. Smith, *J. Chem. Phys.* **126**, 155102 (2007).

³³N. Buchete and G. Hummer, *J. Phys. Chem. B* **112**, 6057 (2008).

³⁴F. Noé and S. Fischer, *Curr. Opin. Struct. Biol.*, **18**, 154 (2008).

³⁵J. D. Chodera and F. Noé, *Curr. Opin. Struct. Biol.*, **25**, 135 (2014).

³⁶C.R. Schwantes, R.T. McGibbon, and V.S. Pande, *J. Chem. Phys.*, **141**, 090901 (2014).

³⁷Y. Naritomi and S. Fuchigami, *J. Chem. Phys.*, **134**, 065101 (2011).

³⁸G. Pe'rez-Hernandez, F. Paul, T. Giorgino, G. D. Fabritiis, and F. Noé, *J. Chem. Phys.*, **139**, 015102 (2013).

³⁹C. R. Schwantes and V. S. Pande, *J. Chem. Theo. Comput.*, **9**, 2000 (2013).

⁴⁰S. Honda, K. Yamasaki, Y. Sawada, H. Morii, *Structure* **12**, 1507 (2004).

⁴¹D. Satoh, K. Shimizu, S. Nakamura, and T. Terada, *FEBS Letters*, **580**, 3422 (2006).

⁴²A. Suenaga, T. Narumi, N. Futatsugi, R. Yanai, Y. Ohno, N. Okimoto, and M. Taiji, *Chem. Asian J.* **2** 591 (2007).

⁴³R. Harada and A. Kitao, *J. Phys. Chem. B*, **115**, 8806 (2011).

⁴⁴P. Kuhrova, A. D. Simone, M. Otyepka, and R. B. Best, *Biophys. J.*, **102**, 1897 (2012).

⁴⁵H. Okumura, *Proteins*, **80**, 2397 (2012).

⁴⁶D. A. Case, T. A. Darden, T. E. Cheatham, III, C. L. Simmerling, J. Wang, R. E. Duke, R. Luo, K. M. Merz, B. Wang, D. A. Pearman, M. Crowley, S. Brozell, V. Tsui, H. Gohlke, J.

Mongan, V. Hornak, G. Cui, P. Beroza, C. Schafmeister, J. W. Caldwell, W. S. Ross, and P. A. Kollman, AMBER8, University of California, San Francisco (2004).

⁴⁷C. Eckart, *Phys. Rev.*, **47**, 552 (1935).

⁴⁸A. D. McLachlan, *J. Mol. Biol.*, **128**, 49 (1979).

⁴⁹See supplemental material at [URL will be inserted by AIP] for additional results of Figs. S1, S2, and S3.

⁵⁰W. Humphrey, A. Dalke, and K. Schulten, *J. Mol. Graph.*, **14**, 33 (1996).

FIGURE CAPTIONS:

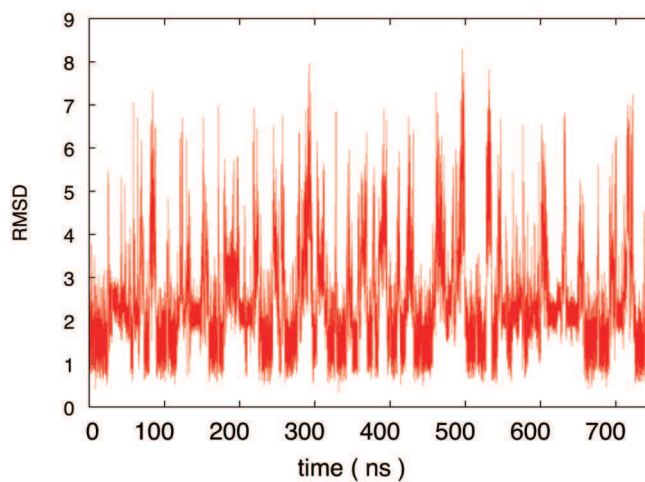


FIG. 1. The time series of RMSD (\AA) from the native structure of chignolin near a transition temperature. There are many transitions among the native-like structures (RMSD $\approx 1 \text{ \AA}$), misfolded structures (RMSD $\approx 2 \text{ \AA}$), and unfolded structures (RMSD $\approx 5 \text{ \AA}$).

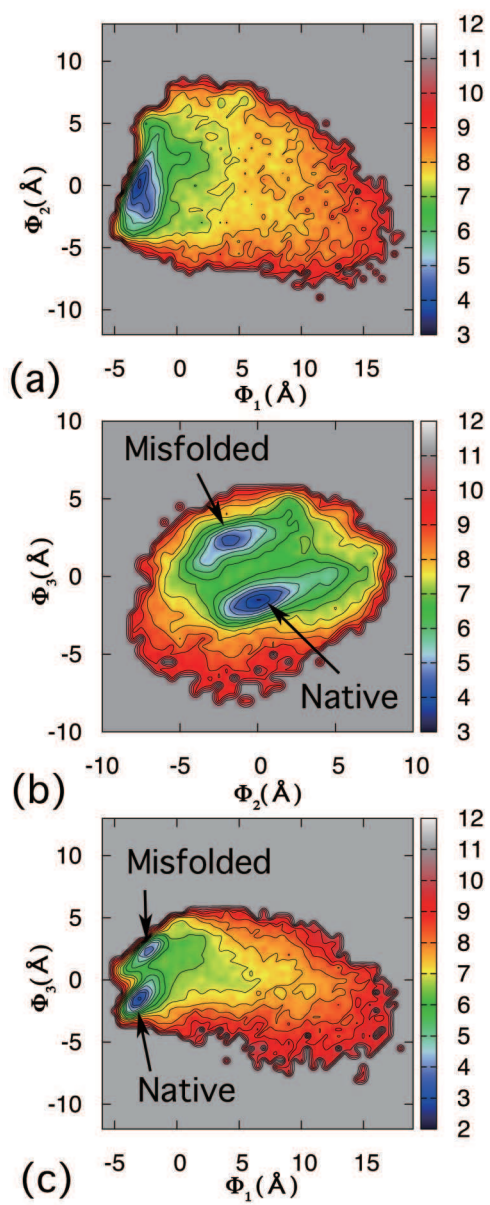


FIG. 2. The free-energy surfaces of (a) Φ_1 and Φ_2 , (b) Φ_2 and Φ_3 , and (c) Φ_1 and Φ_3 .

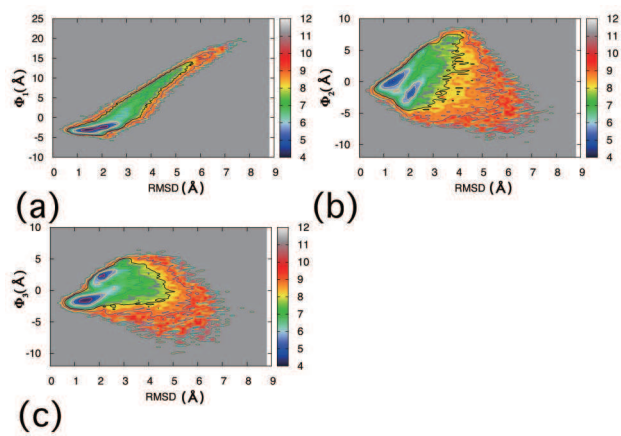


FIG. 3. The relations between RMSD and (a) Φ_1 , (b) Φ_2 , or (c) Φ_3 .

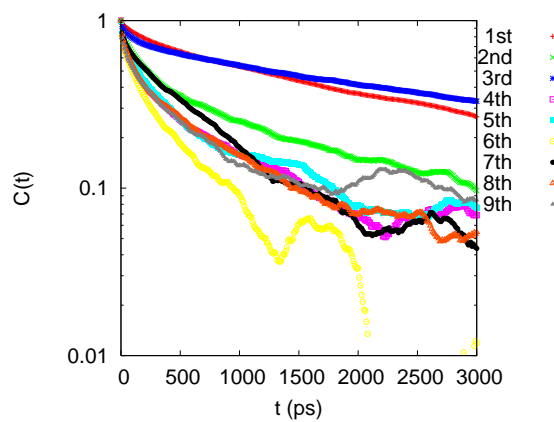


FIG. 4. The time-displaced autocorrelation functions $\langle \Phi_p(t)\Phi_p(0) \rangle$ of Φ_p ($p = 1, \dots, 9$) for PCA.

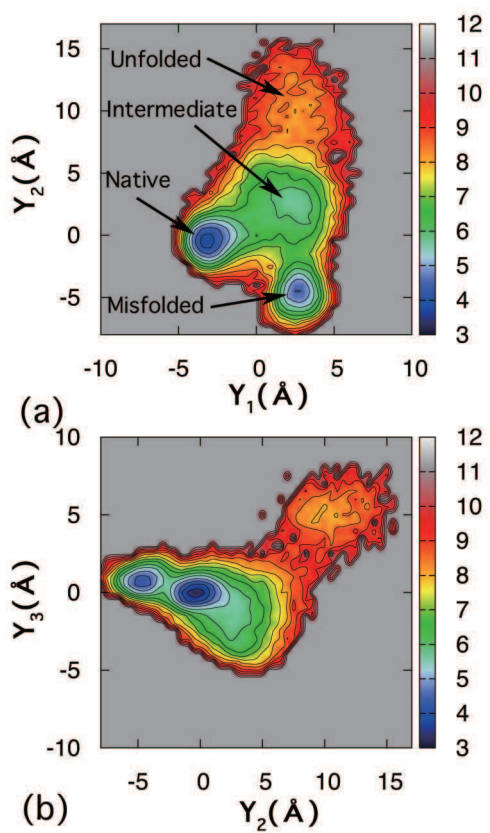


FIG. 5. The free-energy surfaces of (a) Y_1 and Y_2 , and (b) Y_2 and Y_3 for RMA

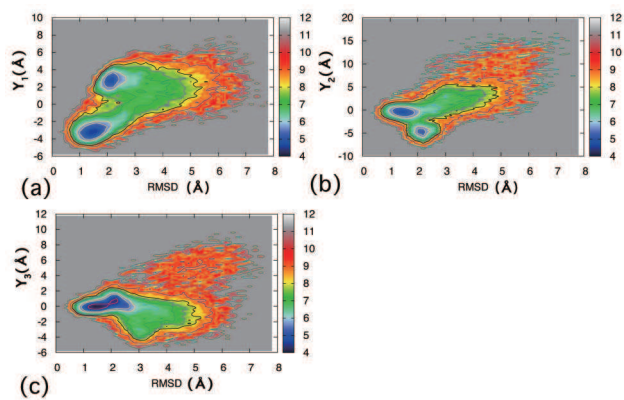


FIG. 6. The relations between RMSD and (a) Y_1 , (b) Y_2 , or (c) Y_3 .

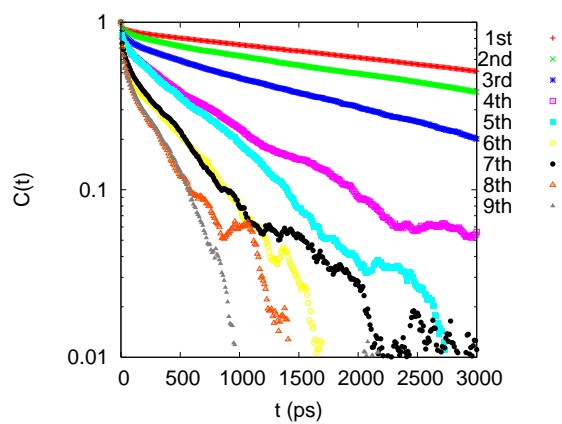


FIG. 7. The time-displaced autocorrelation functions $\langle Y_p(t)Y_p(0) \rangle$ of Y_p , ($p = 1, \dots, 9$) for RMA.

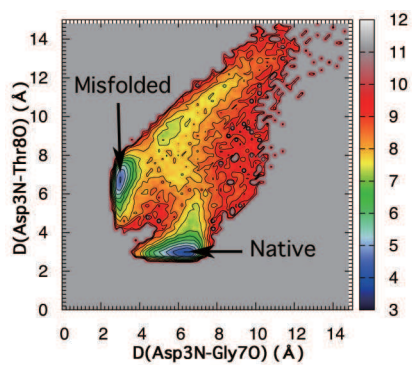


FIG. 8. The free-energy surface along the distances between the amide nitrogen atom of Asp3 and the carbonyl oxygen atom of Thr8, $D(\text{Asp3N-Thr8O})$, and between the amide nitrogen atom of Asp3 and the carbonyl oxygen atom of Gly7, $D(\text{Asp3N-Gly7O})$.

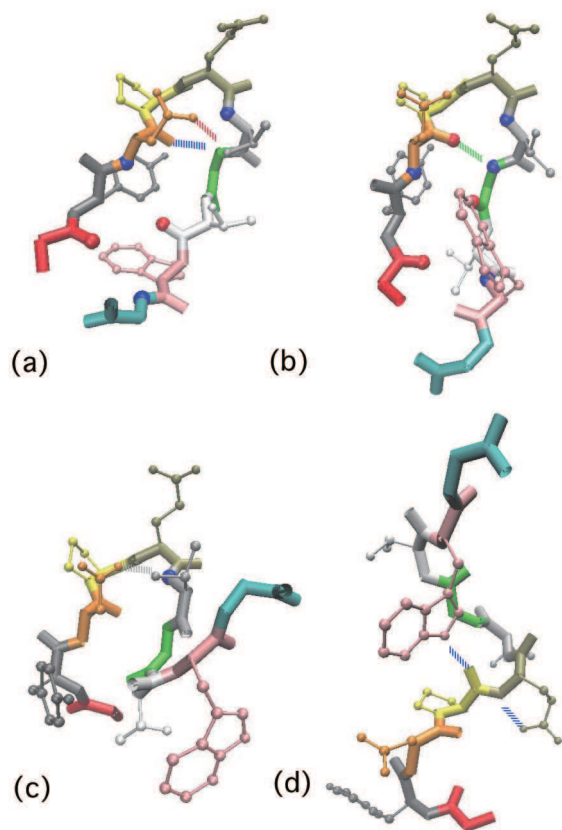


FIG. 9. Structures of the (a) native state, (b) misfolded state, (c) intermediate state, and (d) unfolded state (Multimedia view). The structures are fitted on the backbone atoms from Asp3 to Glu5. The movies of the snapshots are made using Visual Molecular Dynamics (VMD)⁵⁰. The residues of Gly1 and Gly10 are shown in red and cyan, respectively. Some characteristic hydrogen bonds obtained by the Hbonds plugin of VMD with the cut-off distance of 3.0 Å and the cut-off angle of 30 degrees are also shown. Some important oxygen and nitrogen atoms of the backbone are shown as red and blue spheres, respectively.

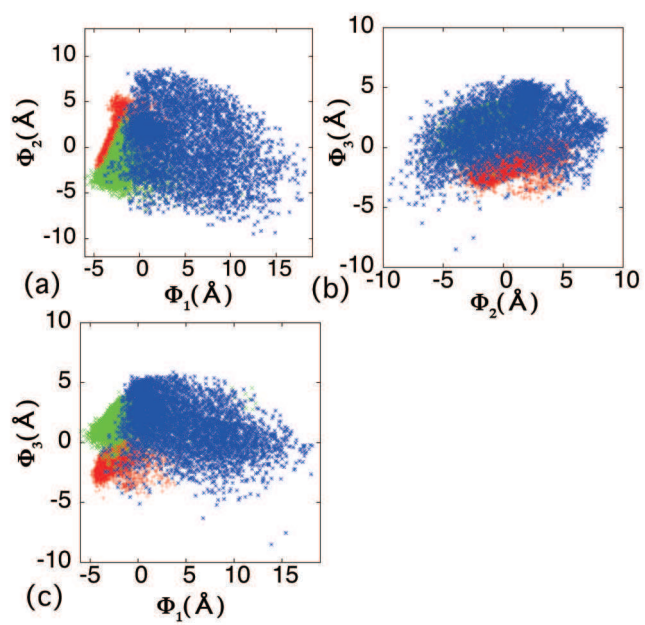


FIG. 10. The distributions for the native state (red), misfolded state (green), and intermediate state (blue) in the planes of (a) Φ_1 and Φ_2 , (b) Φ_2 and Φ_3 , and (c) Φ_1 and Φ_3 .

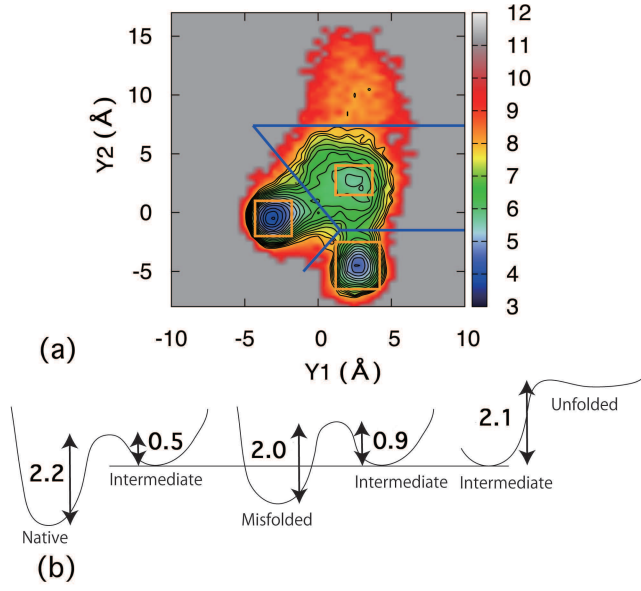


FIG. 11. (a) The free-energy surface of Y_1 and Y_2 showing three regions for the native, misfolded, and intermediate structures listed in Table II (in orange) and the dividing lines for the four states of the Markov state models and the Markov state relaxation mode analysis model (in blue). (b) Schematic drawing of the free-energy differences between the intermediate states and the other three states (native, misfolded, and unfolded states). The contour lines are drawn in the range from 3 to 8 at an interval of 0.25. The values in (b) are $RT \times \Delta F$, where ΔF is the difference of the free energy given by Eq. (19) and RT is 0.89 kcal/mol at $T = 450$ K. The free energy differences are approximately estimated by counting the numbers of contour lines.

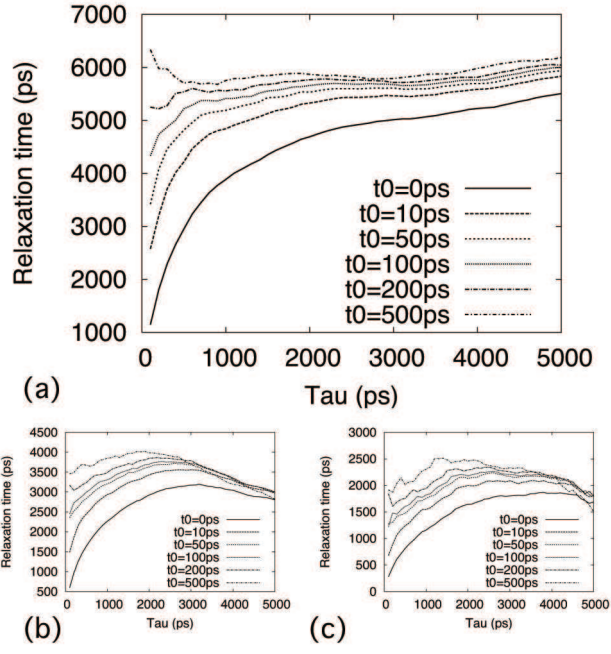


FIG. 12. The relaxation times of the (a) second, (b) third, and (c) fourth relaxation modes obtained by MSRMA as a function of time interval τ . The lines of $t_0 = 0$ ps correspond to the results of a simple Markov state model.

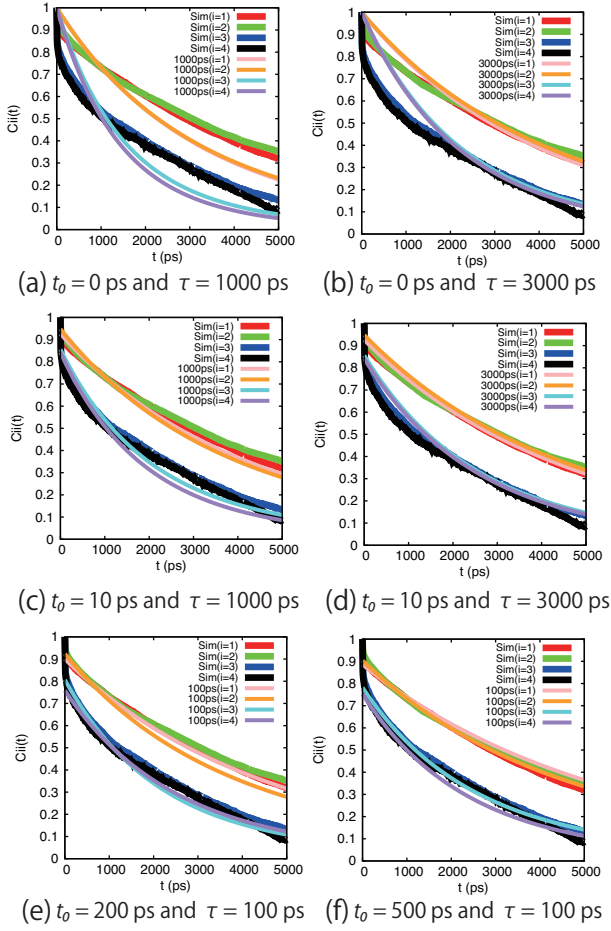


FIG. 13. The normalized time-displaced autocorrelation functions $\hat{C}_{i,i}(t)$ of Eq. (32) calculated directly (Sim) and reproduced by Eq. (14). The values of $t_0 = 0$ and τ in picoseconds are (a) 0 and 1000, (b) 0 and 3000, (c) 10 and 1000, (d) 10 and 3000, (e) 200 and 100, and (f) 500 and 100, respectively. The results of $t_0 = 0$ ps correspond to those of the simple Markov state model.

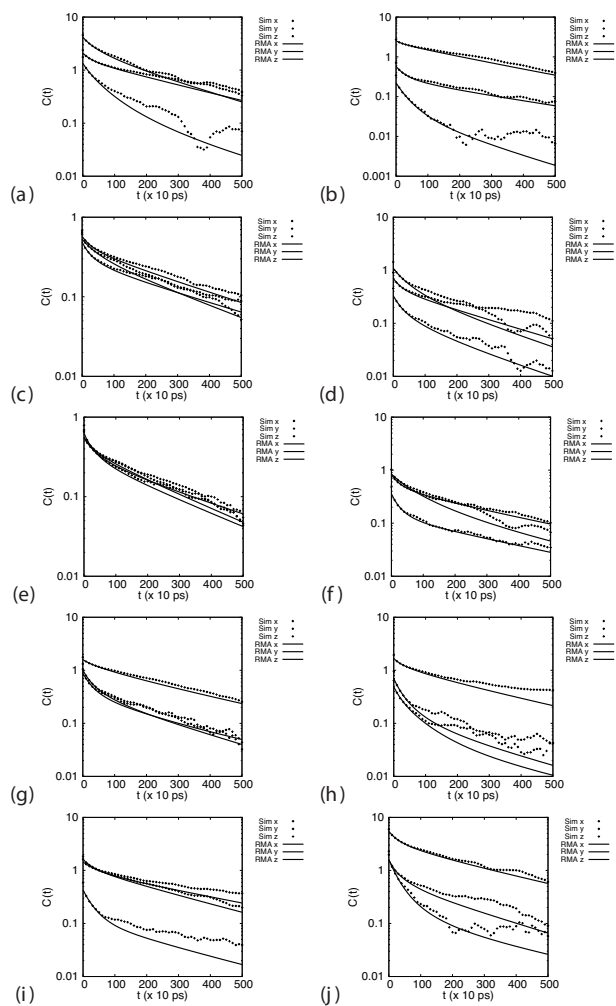


Fig. S1 (Supplemental Material): The time-displaced autocorrelation functions of x,y,z-coordinates for i th C_α atom ($i = 1, \dots, 10$) obtained by the simulation directly (Sim) and reproduced by RMA (RMA).

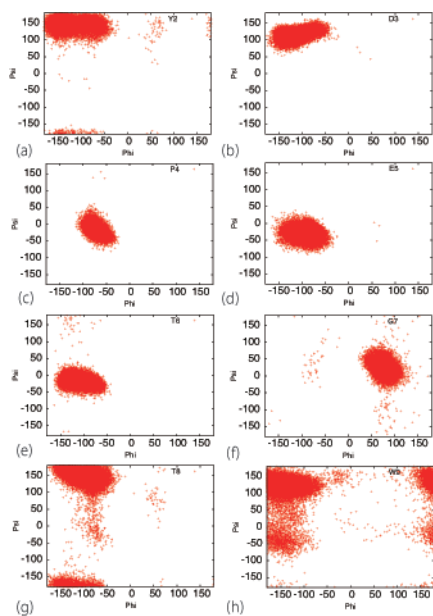


Fig. S2-1 (Supplemental Material): The ramachandran plots of each residue from Tyr2 to Trp9 (from (a) to (h)) of the native state.

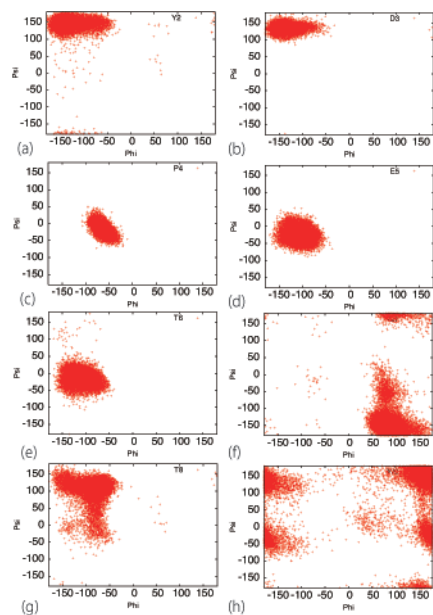


Fig. S2-2 (Supplemental Material): The ramachandran plots of each residue from Tyr2 to Trp9 (from (a) to (h)) of the misfolded state.

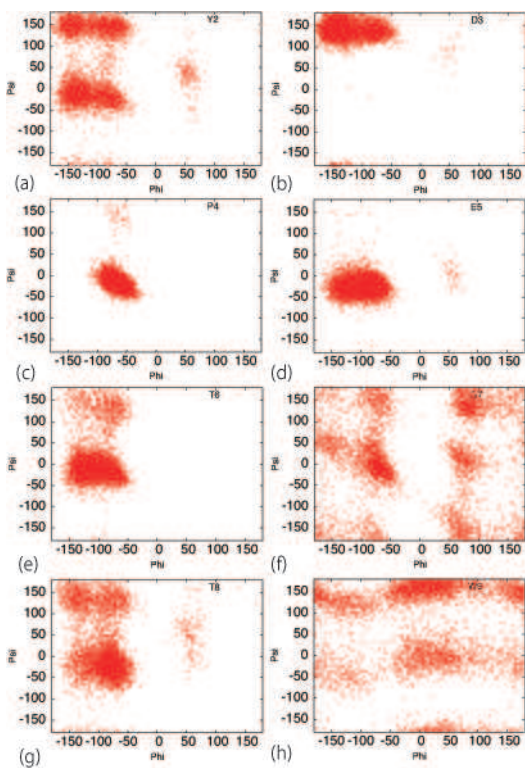


Fig. S2-3 (Supplemental Material): The ramachandran plots of each residue from Tyr2 to Trp9 (from (a) to (h)) of the intermediate state.

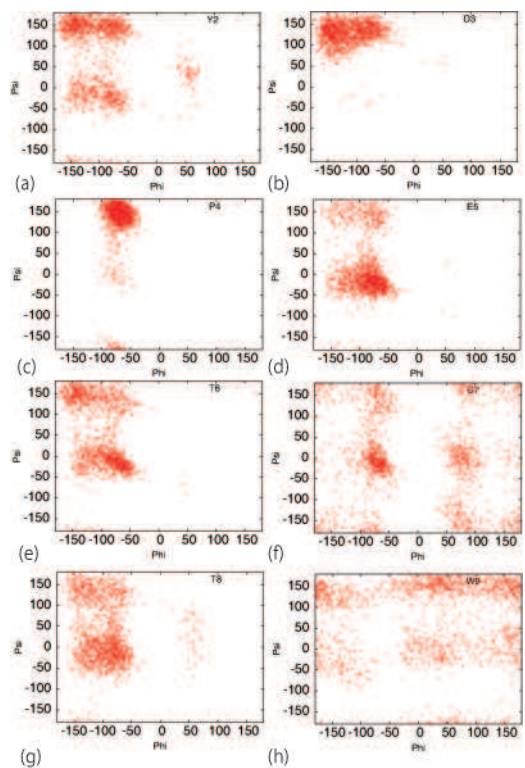


Fig. S2-4 (Supplemental Material): The ramachandran plots of each residue from Tyr2 to Trp9 (from (a) to (h)) of the unfolded state.

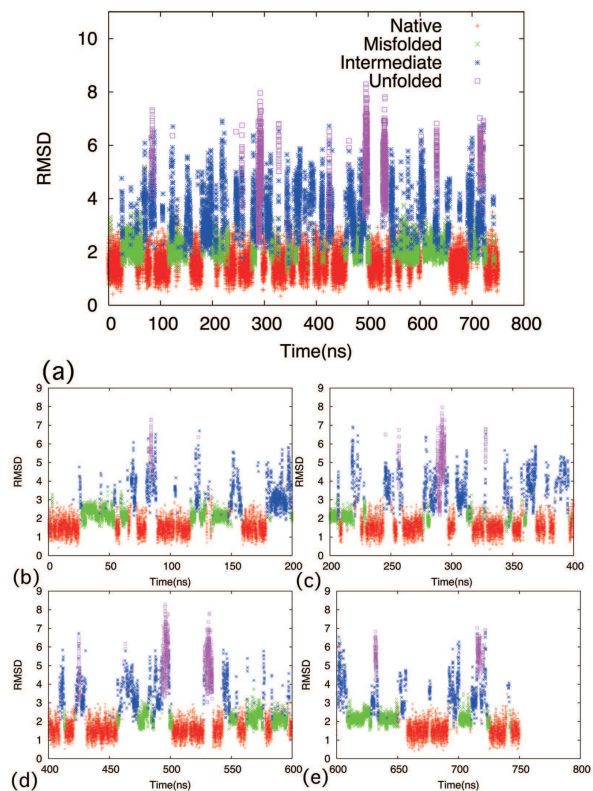


Fig. S3 (Supplemental Material): The time series of the values of RMSD from the native structure for the native, misfolded, intermediate, and unfolded states listed in Table II. The time series of all steps (a), from 200 ns to 400 ns (b), from 400 ns to 600 ns (c), and from 600 ns to 800 ns (d) are shown.